Open Access

Earth System
Science
Data

Discussions

Snow accumulation and ablation measurements in a mid-latitude mountain coniferous forest (Col de Porte, France, 1325 m alt.): The Snow Under Forest field campaigns dataset

Jean Emmanuel Sicart[1], Victor Ramseyer[1], Ghislain Picard[1], Laurent Arnaud[1], Catherine Coulaud[1], Guilhem Freche[1], Damien Soubeyrand[1], Yves Lejeune[2], Marie Dumont[2], Isabelle Gouttevin[2], Erwan Le Gac[2], Frederic Berger[3], Jean Matthieu Monnet[3], Laurent Borgniet[3], Eric Mermin[3], Nick Rutter[4], Clare Webster[5,6], Richard Essery[7].

[1] Univ. Grenoble Alpes, IRD, CNRS, Grenoble INP, IGE, 38000 Grenoble, France.
[2] CNRM UMR 3589, Météo-France/CNRS, Centre d'Études de la Neige, Grenoble, France
[3] Univ. Grenoble Alpes, INRAE, LESSEM, 2 rue de la Papeterie-BP 76, St-Martin-d'Hères, F-38402, France.
[4] Department of Geography and Environmental Sciences, Northumbria University, Newcastle upon Tyne, NE1 8ST, UK
[5] WSL Swiss Federal Institute for Snow and Avalanche Research SLF, Davos, Switzerland
[6] Department of Geosciences, University of Oslo, Norway
[7] School of GeoSciences, University of Edinburgh, UK

Correspondence to: Jean Emmanuel Sicart (jean-emmanuel.sicart@ird.fr)

Abstract. Forests strongly modify the accumulation, metamorphism and melting of snow in mid and high-latitude regions. Recently, snow routines in hydrological and land surface models have been improved to incorporate more accurate representations of forest snow processes, but model inter-comparison projects have identified deficiencies, partly due to incomplete knowledge of the processes controlling snow cover in forests. The Snow Under Forest (SnoUF) project was initiated to enhance knowledge of the complex interactions between snow and vegetation. Two field campaigns, during the winters 2016-17 and 2017-18, were conducted in a coniferous forest bordering the snow study at Col de Porte (1325 m a.s.l, French Alps) to document the snow accumulation and ablation processes. This paper presents the field site, instrumentation, and collection methods. The observations include distributed forest characteristics (tree inventory, LIDAR measurements of forest structure, sub-canopy hemispherical photographs), meteorology (automatic weather station and radiometers array), snow cover and depth (snow poles transect and laser scan), and snow interception by the canopy during precipitation events. The weather station installed under dense canopy during the first campaign has been maintained since then and provides continuous measurements throughout the year since 2018. Data are publicly available from the repository of the Observatoire des Sciences de l'Univers de Grenoble (OSUG) data center at http://dx.doi.org/10.17178/SNOUF.2022 (Sicart et al., 2022).

1 Introduction

Around 20% of Northern Hemisphere snow overlaps with boreal forest, so sub-canopy snow cover has a key control on eco-hydrological processes (e.g., Rutter et al., 2009). Forests strongly modify the accumulation, metamorphism and melting of snow, they intercept part of the precipitation, modify radiation fluxes and surface roughness, and reduce albedo and wind speed (e.g., Otterman et al., 1988; Pomeroy et al., 2008; Musselman et al., 2012; Essery, 2013). The model inter-comparison project SNOWMIP2 (Essery et al., 2009; Rutter et al., 2009) evaluated 33 forest snow models differing in both process complexity and canopy implementation approaches. Major deficiencies of modeling snow in forests were identified, and the project concluded that model performance was limited by incomplete knowledge of the processes controlling snow cover in forests. Since then, numerous measurement campaigns have been conducted (e.g., Webster et al. 2016, 2018; Malle, et al., 2019; Mazzotti et al., 2019; Hojatimalekshah et al., 2021) and snow routines in hydrological and land surface models have been enhanced to incorporate more accurate representations of forest snow processes (e.g., Ellis et al., 2013; Gouttevin et al., 2015; Boone et al., 2017; Mazzotti et al., 2020). However, these improved routines still represent canopy as one homogeneous layer without accounting for all the effects of particularly vertical canopy heterogeneity on snow accumulation and ablation processes. Detailed snow and meteorological measurements are therefore still required, and remain an important step, to better understand the complex interactions between snow and vegetation. Col de Porte (CDP) is a mid-elevation site located at 1325 m altitude (45.3° N, 5.77° E) in the Chartreuse mountain range in France, with a meadow bordered by a coniferous forest. Morin et al. (2012) and Lejeune et al. (2019) presented the meadow observation site that has been operated since 1959 by CEN-MeteoFrance. Daily measurements of snow depth, air temperature, and precipitation amount have been performed since 1960. Hourly measurements of meteorological and snow variables required to run and evaluate detailed snowpack models such as Crocus (Vionnet et al., 2012) started in 1987 and have been almost continuous during the snow seasons since 1993. CDP is part of several observation networks at the national scale (e.g., Observation pour l'Experimentation et la Recherche en Environnement CryObsClim and Systèmes d'Observation et d'Expérimentation au long terme pour la Recherche en Environnement des glaciers, GlacioClim) and at the international scale (e.g., ILTER European Research Infrastructure, WMO Global Cryosphere Watch CryoNet network, GEWEX INARCH). For more details, the reader is referred to Lejeune et al. (2019). Only a few studies have investigated the snow cover distribution in the forest of CDP (e.g., Durot, 1999); however, the immediate proximity of the forest parcel to the historical, long-term open-area snow observatory of CDP offers a good opportunity to understand and relate the sub-canopy meteorological and snow processes to their open-area counterparts.

Two field campaigns have been conducted in the conifer forest bordering the reference meadow site to document the snow accumulation and ablation processes: from 16 January 2016 to 21 March 2017 and from 1 December 2017 to 15 March 2018. This paper presents the measurement methods that were applied in the forest plot during these two field campaigns. The observations include distributed forest characteristics (tree inventory, LIDAR measurements of forest structure, sub-canopy hemispherical photographs), meteorological variables (automatic weather station and radiometer array), snow height and water equivalent (snow poles transect and laser scan), and transects of snow interception by the canopy during precipitation events.

Earth System
Science
Data

Open Access

Discussions

62 The dataset also includes continuous measurements from the weather station in the forest from March 2018 to June 2022.

63 Complementing the datasets, the repository of the Observatoire des Sciences de l'Univers de Grenoble data center also includes

64 technical information, photographs and a detailed plan of the instrumentation.

2 Site and forest description

2.1 Site

67 The study site is a triangular forest parcel of 2000 m^2 (Figure 1) next to the meadow where the historical open-area snow

68 measurements are conducted. It is delimited by a fence along its south and northeast sides. Its west side corresponds to the

69 edge between the forest and the open meadow area. The terrain slope is around 10° oriented toward east-north-east. The stand

70 is dominated by Norway spruce (*Picea abies*). Young silver firs (*Abies alba*) are present, mainly in the western part of the

71 parcel. Some broadleaved trees are located along the west edge. The parcel exhibits two gaps in the canopy. The smallest one

72 is in the south-west, while the larger one is at the center and extends toward the south fence (Figure 1). During the first [second]

73 campaign, the annual maximum snow depth was around 100 cm [160 cm] in the open site (meadow reference site) and only

74 around 50 cm [130 cm] under the canopy.

Earth System
Science
Data
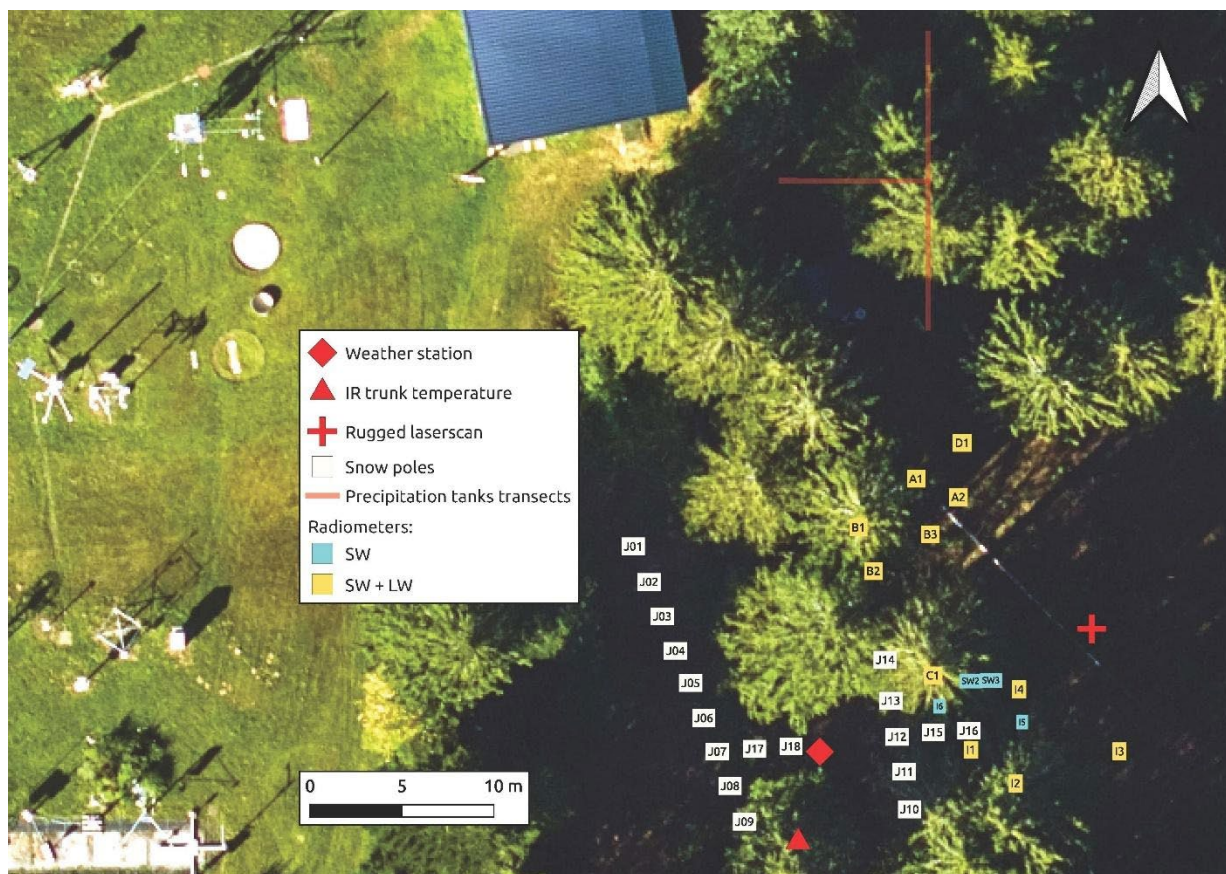
Figure 1: Aerial photograph of the site with locations of the sensors. The sensors of the open meadow area appear on the left of the picture.

2.2 Forest measurements

2.2.1 Forest inventory

An inventory of trees higher than 1.3 m took place during field campaigns between September 2016 and July 2018. On 13-14 September 2016, live and dead trees were inventoried, and the following observations and measurements were performed:

- diameter at breast height (DBH, measured with a tape measure at 1.3 m height above the ground, upslope of the tree),
- species,
- tree height measured with a Haglöf Vertex 4 hypsometer, only for trees with a DBH larger than 7.5 cm.

Tree identification numbers were painted on the trunk at a height around 1.3 m above ground. Three reference poles were positioned in the site and geolocated using a Trimble GeoExplorer 6000 XH GNSS receiver. Trees were mapped relative to a nearby pole by measuring the ground distance (Vertex 4 hypsometer), slope (clinometer) and azimuth (compass). Tree position

90   precision relative to the reference pole is expected to be better than 50 cm, whereas GNSS precision under the forest canopy

91   is of the order of a few meters. 141 trees were inventoried: 128 live trees, 3 dead trees and 10 stumps.

92   On 5 May 2017, vertical crown projections of live trees with a DBH larger than 7.5 cm were measured with a tape measure as

93   the horizontal distances between the trunk center and the vertical projection of the furthest live branch along north, south, east

94   and west directions. If several tree stems were sprouting from a common base, the whole clump was considered to have one

95   single crown and its extension was measured from the stem with the largest diameter in the clump.

96   On 20 June 2017, tree positions were measured with a Leica TS02 total station located in the open area at the west of the forest.

97   The total station position was recorded with a Trimble R2 differential GNSS receiver, ensuring centimetric accuracy.

98   On 27 July 2018, heights and crown extensions were measured on trees with a DBH smaller than 7.5 cm. The tree inventory

99   was extended outside the southern fence to include trees which might cast shadows inside the forest parcel (DBH, height,

100   crown extension, species). Their positions were measured with slope (clinometer), azimuth (compass) and ground distance

101   (Vertex 4 hypsometer) relative to a reference pole located with a GNSS receiver.

102   Tree easting and northing values in the RGF 93 - Lambert 93 projected coordinate system were then derived from the total

103   station coordinates if available, or from their polar coordinates relative to a reference pole. Tree altitude values were computed

104   from the airborne laser scanning data (see Section 2.2.2) by bilinear interpolation of the ground-classified points at the location

105   of trees. Figure 2 shows a map of inventoried live trees and canopy heights. In the forest stand inside the fence, most of the

106   trees are between 30 and 40 m high (Figure 3) and the total basal area is about 66.3 m2/ha. It includes 52 firs, 43 spruce and

107   33 broadleaved trees. Trees measured outside the southern fence are 9 spruce, 2 firs and 7 broadleaves.

108   Tree position accuracy is estimated to be better than 10 cm for the trees measured with the total station inside the fenced area

109   (it is estimated to be around 50 cm for additional trees outside the fence). Luoma et al. (2017) reported a precision of 0.5 m

110   (standard deviation) for height measurements with a Vertex 4 clinometer. Elzinga et al. (2005) reported a standard deviation

111   of 0.5 cm for diameters measured with a tape measure. Measurement errors on crown extension is mostly due to the difficulty

112   to assess the vertical projection of the branches' extent on the ground. Accuracy is expected to be from 10 cm for small trees

113   (height smaller than 4 m) to 50 cm for the tallest ones (around 30 m).

114
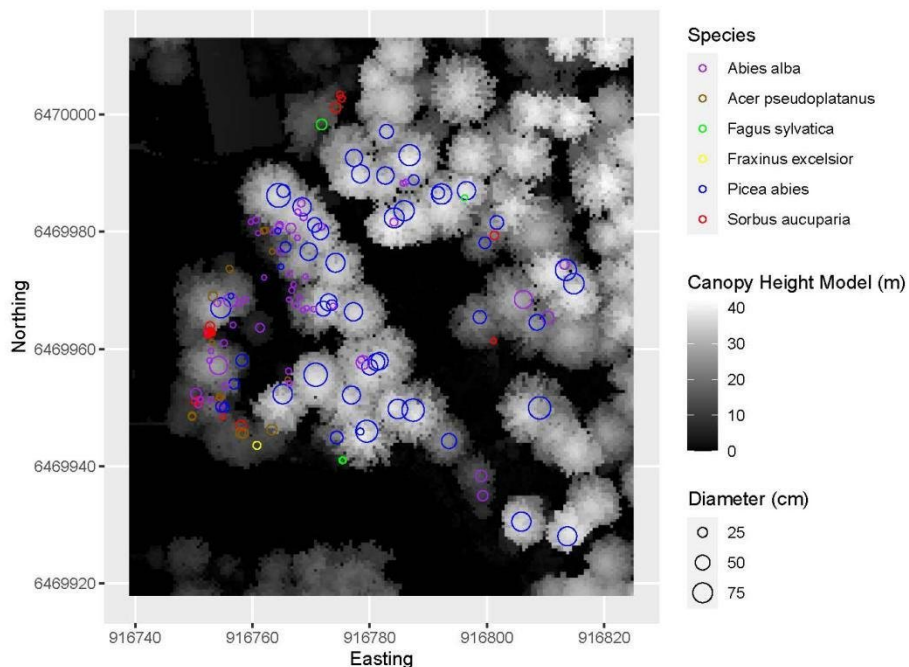
115

116   Figure 2. Map of inventoried live trees and canopy height model derived from airborne laser scanning.
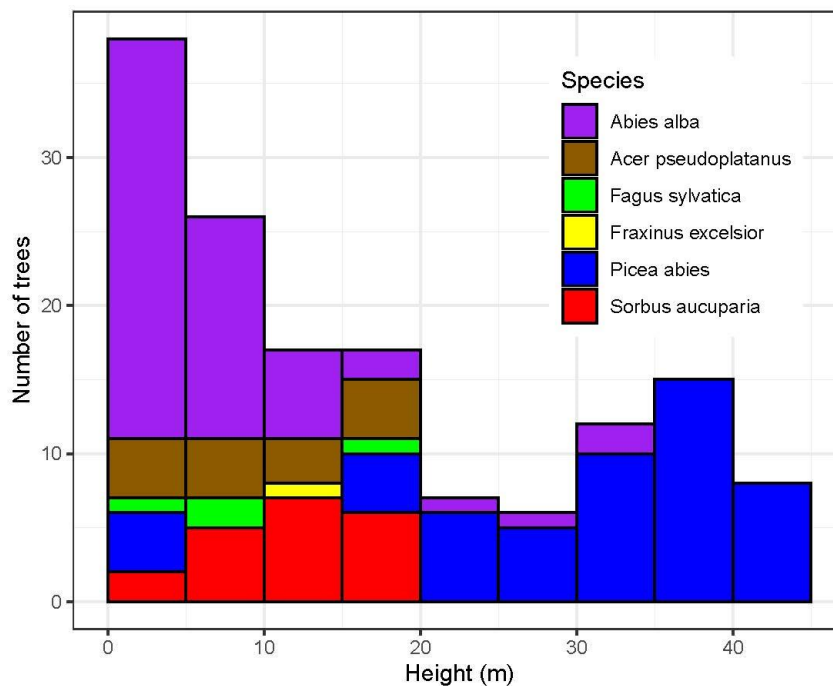
117

118   Figure 3: Height distribution of living trees.

119

120   *2.2.2 Airborne remote sensing measurements*

121   Airborne laser scanning (ALS) is a remote sensing technique based on LIDAR which can provide a 3D point cloud of forest

122   structure. The geometric information on the vegetation can be processed to derive forest metrics used to parametrize snow

123   interception (e.g., Helbig et al., 2020). ALS was acquired during a campaign covering 123.5 km^2 between 30 August and 2

124   September 2016, using a Riegl LMS Q680i sensor mounted on a helicopter. The scheduled flight height and speed were 750 m

125   above ground and 70 knots, respectively. The scan frequency was 300 kHz with a scan angle of $\pm$ 30°. The aircraft trajectory

126   was computed from the Inertial Measurement Unit and GPS data. Point coordinates were extracted and computed using the

127   RiAnalyse and RiWorld software. The point cloud was then classified as ground / non-ground using Terrasolid.

128   To assess the accuracy on elevation measurements, 318 ground control points were measured with differential GNSS in 11

129   flat, vegetation-less plots. Differential GNSS accuracy is around 2-3 cm in such areas. Comparison of the control points with

130   the point cloud yielded to an altitudinal accuracy of 4.7 cm (root mean square error of differences), with a bias of -0.3 cm.

131   The point cloud was delivered in tiled LAS 1.2 files. The coordinate system was RGF 93 - Lambert 93, with altitude in the

132   system NGF-IGN69. The point cloud corresponding to the study site with a 200 m buffer was exported in a single compressed

133   LAS file (v1.1 format 1). Pulse density in the study site is 17 points/m^2, resulting in densities of 3.3 points/m^2 for ground points

134   and 28 points/m^2 with multiple returns for canopy points. The area located more than 30 m to the southeast of the study area

135   was not covered by the acquisition.

136   For the extent of the inventoried trees plus a 30 m buffer, digital surface models were computed at 0.5 m resolution from the

137   ALS point cloud. The digital terrain model (DTM) was computed by estimating the altitude of each cell center by bilinear

138   interpolation of ALS points classified as ground. The point cloud was normalized by subtracting the ground altitude at the

139   position of each point, estimated by bilinear interpolation of ground points. A canopy height model (CHM) was computed by

140   retaining the highest value of normalized heights in each cell. Cells without values were filled by the median of their 3x3

141   neighborhood. The DTM and CHM were delivered as raster files in tif format. Aerial photographs were also taken during the

142   ALS acquisition. Pictures were used to produce a 10 cm resolution RGB orthophoto provided as a tif file for the extent of the

143   DTM. Figure 4 shows a perspective view of the 3D point cloud acquired by the airborne laser scanning.

144

Earth System
Science
Data
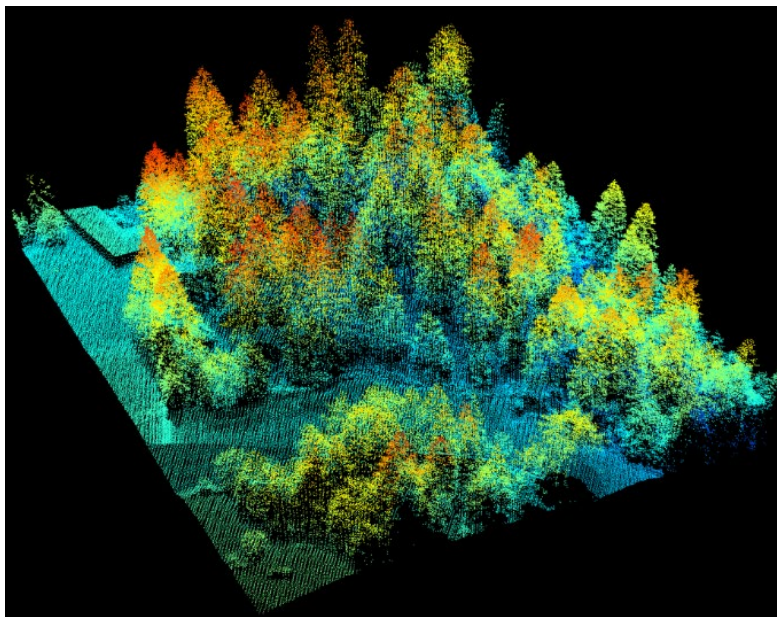
Figure 4: Perspective view of the 3D point cloud acquired by airborne laser scanning. Points are colored according to their altitude.

2.2.3 Hemispherical photographs

Hemispherical photographs were taken on 4 September 2017 at the weather station and at each radiometer in homogeneous overcast conditions to ensure spatially uniform sky brightness. A Nikon Coolpix 4300 digital camera was used with a Nikon FC-E8 fisheye lens, mounted 60 cm above the ground surface on a tripod. The camera was aligned to north with a compass and carefully levelled using a bubble level. There was no snow in the canopy. Sky view factors were then calculated following Essery et al. (2008) assuming an equiangular lens projection. To distinguish vegetation from sky pixels, and to calculate the sky view factor at each location, a brightness threshold was visually adapted to each hemispherical photograph (Figure 5). This allows us to account for variations in illumination conditions during changes in cloud cover or thickness. As a result, the calculated sky view factor ranges from 0.15 to 0.35 at the radiometer sites, mostly situated under a rather dense canopy. Reid et al. (2014) estimated the uncertainty in the sky view factor using this method to be ±0.02.

Figure 5: Example of a hemispherical photograph (left) and a binary image (right, calculated sky view factor 0.25). The photograph was taken on 4 September 2017 at radiometer A1 (Figure 1).

2.3 Meteorological and snow observations in the forest

2.3.1 Radiometer array

An array of 13 CMP3 Kipp & Zonen pyranometers and 11 CGR3 Kipp & Zonnen pyrgeometers was deployed on the snow surface from dense canopy to an opening (Figure 1). During the first campaign, each radiometer was positioned horizontally with a bubble level on a wooden board placed on the snow surface. During the second campaign, the horizontal support of the radiometers was attached to a vertical bar fixed in the ground. The height of the support was adjusted to the snow surface every two or three days. This system allowed better stability and levelling of the radiometers. One-minute averages of the incoming radiation fluxes measured at five second time intervals were recorded by two Campbell Scientific CR3000 data loggers. Inter-calibration of the sensors before the campaigns led to estimates of sensor accuracies close to those announced by the manufacturer: ± 12 W m^{-2} for solar radiation and ± 8 W m^{-2} for longwave radiation, in accordance with uncertainty estimations from similar sensors of Halldin et Lindroth (1992), Philipona et al. (2001), Michel et al. (2008), or Van den Broeke et al. (2004). The radiation data were carefully post-processed to remove periods when the sensors were snow covered or tilted.

2.3.2 Weather station

The weather station was installed under rather dense canopy during the first campaign and has been maintained since then. Table 1 lists the sensors installed on the station, their specifications and their accuracy according to the manufacturer. The ultrasonic depth gauge measures the snow height. Ten temperature probes buried in the ground are used to estimate the heat conduction flux. 15-minute averages of the data measured at 10 second time intervals are recorded by a Campbell Scientific CR3000 data logger. An AXIS M1125-E camera took pictures of the surface around the weather station every three hours

183   during daytime. These images are used to monitor surface and sensor conditions. A Campbell Scientific IR120 infrared sensor

184   was used to measure the surface temperature of a trunk close to the meteorological station (Figure 1). One-minute averages of

185   longwave irradiance measured at five second time intervals were recorded by a Campbell Scientific CR1000 data logger.

186

187   Table 1: variables measured by the weather station below the canopy along with the sensor type, heights and precision

188   according to the manufacturer.

Quantity	Sensor Type	Height (cm)[1]	Accuracy according to the manufacturer
Air temperature, °C and relative humidity, %	Campbell CS215C	210	±0.2 °C ±2% in [0-90%] ±3% in [90-100%]
Wind speed and direction, m s^{-1} and deg.	Gill windsonic	210	±0.3 m s^{-1} ±3 deg
Incident and reflected short-wave radiation, W m^{-2}	Kipp & Zonen CM3 0.3<λ<2.8 μm	100	±10% for daily sums
Incoming and outgoing long-wave radiation, W m^{-2}	Kipp & Zonen CG3 5<λ<50 μm	100	±10% for daily sums
Surface elevation changes, mm	Ultrasonic depth gauge Campbell SR50	180	±1 cm
Temperature in the ground, °C	108 Campbell	-2.5, -8, -15, -30, -60[2]	≤ ±0.01°C

189   [1] height above snow-free ground

190   [2] two sensors for each depth

191

192   As an example of the use of these measurements, Figure 6 shows hourly changes in air and soil temperatures and snow depth

193   from December 2018 through May 2019, a winter characterized by deep and sustained snow cover. Snow cover began to build

194   in late December, reaching a maximum of 90 cm in early February. Melt rates became significant as air temperatures remained

195   consistently above 0°C through late February. Snow cover disappeared by the end of March, although there were a few

196   snowfalls through May. Snow cover strongly affected soil temperatures to a depth of 60 cm. The disappearance of the main

197   snow cover at the end of March suddenly reversed the temperature gradient in the soil. Soil temperatures were also affected

198   by a few snowfalls in April, associated with short periods of cold weather.

199
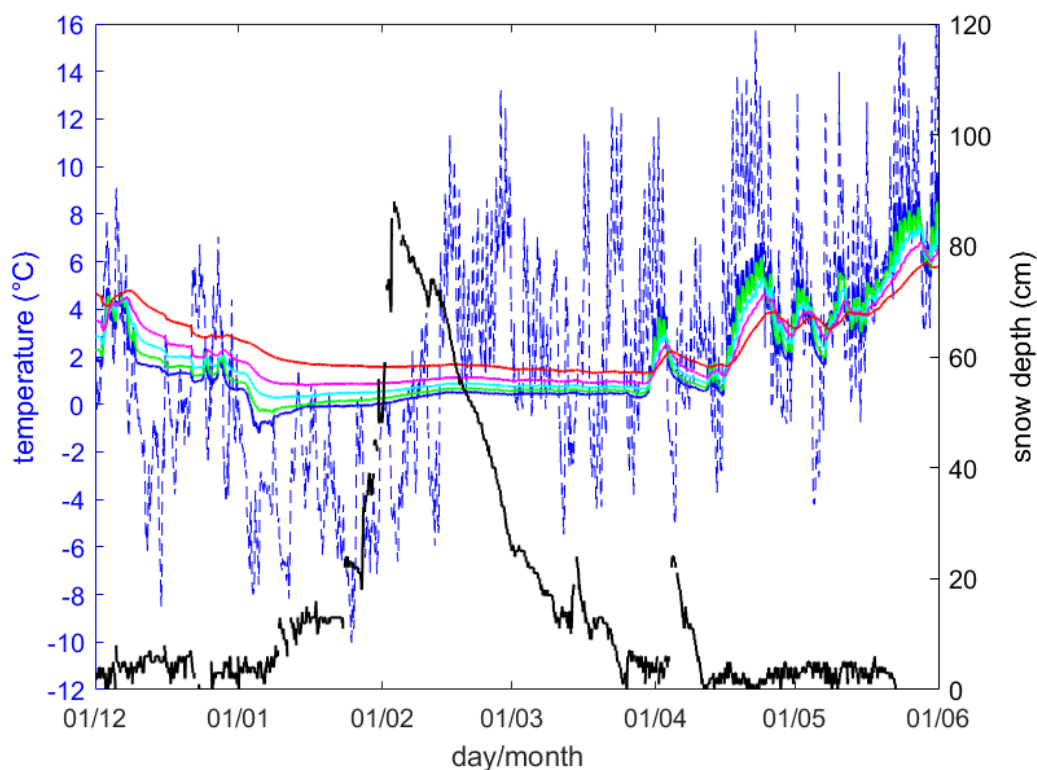
Figure 6: Left Y axis: air temperature (blue dotted line) and soil temperature at 2.5, 8, 15, 30 and 60 cm depth (blue, green, cyan, magenta and red solid lines, respectively). Right Y axis: snow depth (black line). Hourly data from the weather station in the forest (Table 1) from 1 September 2018 to 1 June 2019.

2.3.3 Snow measurements

In order to document the spatial variability of snow cover in the forest, a transect of 18 snow poles was deployed in early winter 2016-2017 (Figure 1). The locations of these snow poles (spaced 2 m apart) were georeferenced in Lambert 93 coordinates. The snow height was measured approximately every two weeks during the two field campaigns. Snow water equivalent measurements were carried out every week for only four poles at a time, alternating among the 18 poles, to minimize destruction of the local snowpack structure. Detailed studies of Morin et al. (2012) and Lejeune et al. (2019) estimated the uncertainties on snow depth and snow water equivalent measurements to be ± 1 cm and ± 5 %, respectively, in agreement with the estimation of López-Moreno et al. (2020) derived from a comparison of measurements with different snow core samplers. Simultaneously, measurements of snow height and water equivalent were made in the reference meadow site as described in Lejeune et al. (2019).

2.3.4 Precipitation tanks

217   The amount of snow held in a forest canopy can be large and remains difficult to measure. Due to the sublimation of intercepted
218   snow, a large portion of the snow retained in the canopy never reaches the ground, and the interplay of interception, sublimation
219   and delayed deposition on the ground creates significant below-forest heterogeneity in snow accumulation (e.g., Helbig et al.,
220   2020). To try to measure snow interception by the canopy, 24 "precipitation tanks" (1 m x 0.39 m) were built and then deployed
221   under the canopy in three eight-meter transects at the start of winter 2017-2018 (Figures 1 and 7). The uncertainties of this
222   new measurement method developed by the CEN is difficult to estimate. Vincent (2018) estimated the measurement
223   uncertainty at about 5%, but additional studies are required to specify it. The mass of snow collected by the precipitation tanks
224   was measured seven times from 20 February to 3 April 2018.

225

227   Figure 7: Precipitation tanks installed below the canopy (photograph by Y. Lejeune).

228

229   *2.3.5 Rugged Laser Scan*

230   The Rugged Laser Scan (RLS) is a scanning laser meter that was installed at about 4 m above the ground close to the center
231   of the main clearing to monitor spatio-temporal variations of snow depth under various canopy covers on a daily or two-daily
232   basis (Figure 1). The device is described in detail in Picard et al. (2016) and is specially designed to monitor snow heights. It
233   comprises a laser meter mounted on a 2-axis stage and can scan ≈ 200000 points in 4 hours. The laser meter was used in scan
234   mode. With a setup at 4 m height, and azimuth angles varying from -90° to +90° and zenith angles varying from 19° and 62°,
235   the scanned area is a half-disk of radius ~7 m, with a surface area of about 80 m^2. The area encompasses three pairs of
236   radiometers installed on the snow surface. Data acquired by the laser meter for a given day are processed to build a cloud of
237   x, y, z points, which is then interpolated and averaged on a regular 3-cm grid. The grid is common to all measurement days so

238   it is easy to compare the evolution of the snow surface. The vertical precision was evaluated to be about 3 mm and the accuracy

239   to be 1 cm (Picard et al. 2016).

240   The RLS was operated during the two field experiments. The first season was from 22 February 2017 to 4 April 2017 (42

241   days) and had 42 valid acquisitions (once a day). The second season was from 5 December 2017 to 11 March 2018 (160 days)

242   and has 81 valid acquisitions because scans were scheduled every other day during the winter (accumulation period) and every

243   day during the melt season. Figure 8 shows an example of snow depths on 15 April 2018 and Figure 9 shows the changes in

244   daily spatial averages of the snow depth during the 2017-18 field campaign.

245
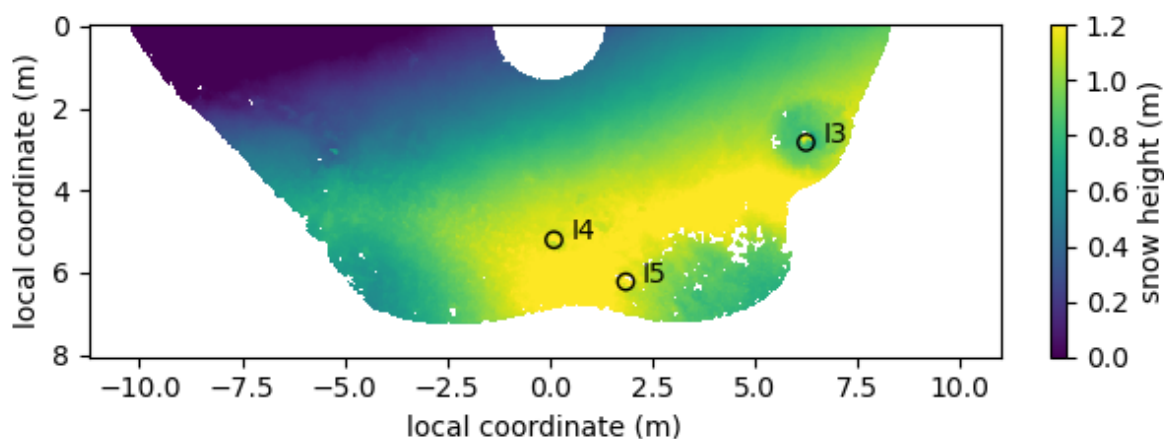
246

247   Figure 8: Snow depths (m) derived from the digital terrain models (DTM) measured by the rugged Laserscan, obtained by

248   subtracting the snow-free DTM from the 15 April 2018 DTM. The measurement area encompasses three radiometers (I3, I4

249   and I5).
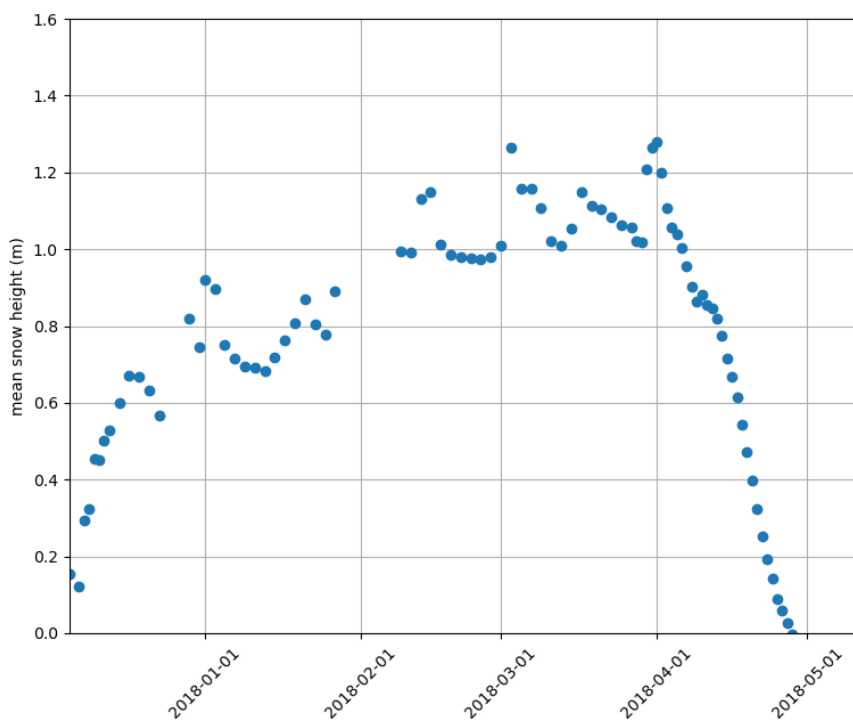
250
251   Figure 9: Daily spatial averages of the snow depth measured by the rugged Laserscan during the 2017-18 field campaign.

252 **3 Spatial variability, measurement uncertainties and data validation**

253 This section provides estimations of the dataset uncertainties related to measurement uncertainties and spatial variability of

254 the variables within the measurement plot. The uncertainties on the sensors and on the measurement methods have been

255 described in the previous sections. For meteorological measurements, sensor manufacturers generally provide reliable

256 information on sensor accuracy (Table 1). In this Section, comparisons of radiation, air temperature, and snow measurements

257 at different locations provide a better insight into the measurement uncertainties and a first validation of the data set.

258 Figure 10 illustrates the spatial variability of the incoming shortwave and longwave radiation fluxes below various forest

259 covers. It shows the effects of clouds and canopy cover on the sub-canopy 15-min radiation fluxes during an overcast day and

260 a clear sky day of the 2017 campaign. Under thick cloud cover (January 31), shortwave radiation, mostly diffuse, reaching the

261 ground remains small but steadily increases with decreasing canopy cover (increasing sky view factor). Sky and vegetation

262 were characterized by similar temperature and longwave emittance (both close to 1), and all the pyrgeometers recorded similar

263 longwave radiations fluxes (within a few of W m^{-2}, confirming the good accuracy of the sensors), without relation with the

264 canopy cover. In clear sky (February 18), shortwave irradiance is mostly direct. Sun flecks on the ground below the canopy

14

265   caused peaks of shortwave irradiance of various amplitudes and at different times at the different pyranometers, superimposed

266   on the spatially constant diffuse shortwave radiation that has penetrated through the canopy. The diurnal changes of sub-

267   canopy longwave irradiance are remarkably parallel between the different measurement sites. The constant offset between the

268   signals is related to the canopy cover due to the large contrast between the large emittance of vegetation and the small emittance

269   of clear, cold sky: the larger the sky view factor, the smaller the longwave irradiance.

270
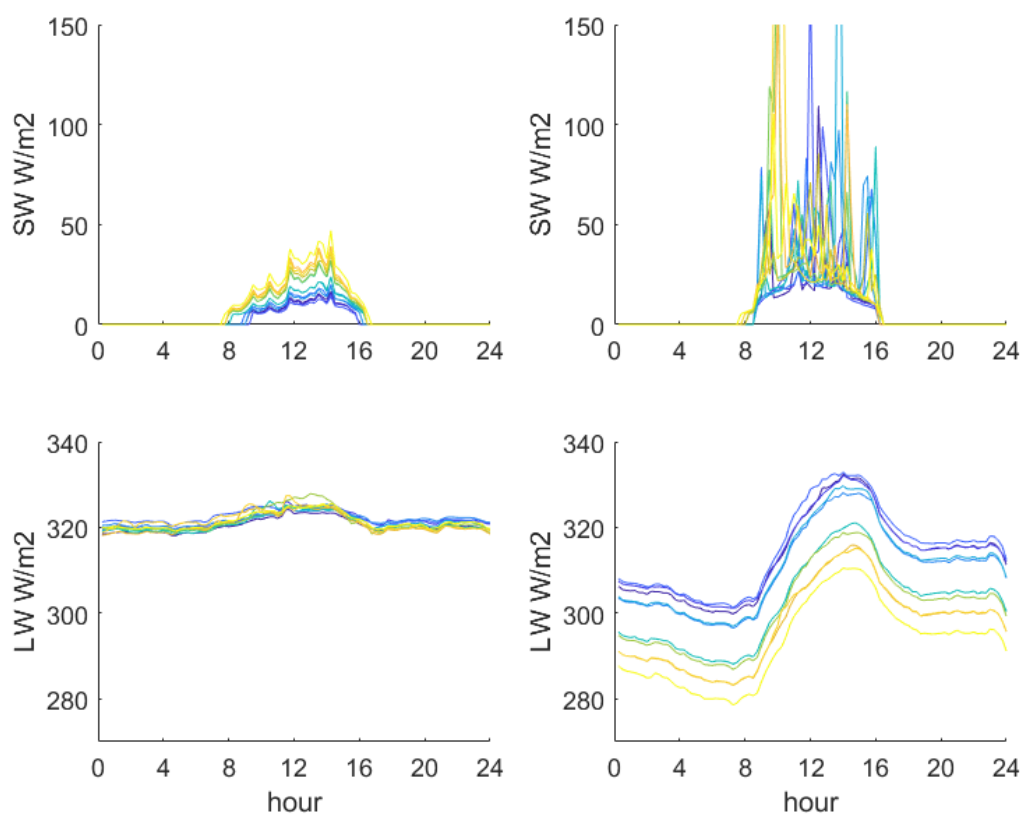
271

272   Figure 10: Shortwave (a, b) and longwave (c, d) incoming radiation fluxes measured by each radiometer during an overcast

273   day (January 31: a, c) and during a clear-sky day (February 18: b, d). 15-min averages of the sub-canopy fluxes during the

274   2017 campaign. Line color is related to the sky view factor V_f from dark blue (lowest $V_f = 0.17$) to yellow (highest

275     $V_f = 0.32$).

276

277   Figure 11 illustrates the hourly air temperature differences between forest and meadow. During daytime, the forest generally

278   is a few degrees colder than the open meadow site, with the difference increasing on clear sky days when air is the warmest

279   (high T_{open}). During the night, the forest is generally slightly warmer than the meadow, with the difference reaching a few

Earth System
Science
Data

Open Access

Discussions

280   degrees on cold clear-sky nights (low T_{open}). Thus, on average, air temperature is quite similar in the forest and the meadow

281   site ($dT \sim 0.2$°CK on average during the 2018 campaign): warmer nights counterbalance cooler days in the forest relative to

282   the meadow. In addition, warmer cloudy periods tend to counterbalance cooler clear-sky periods in the forest relative to the

283   meadow.

284
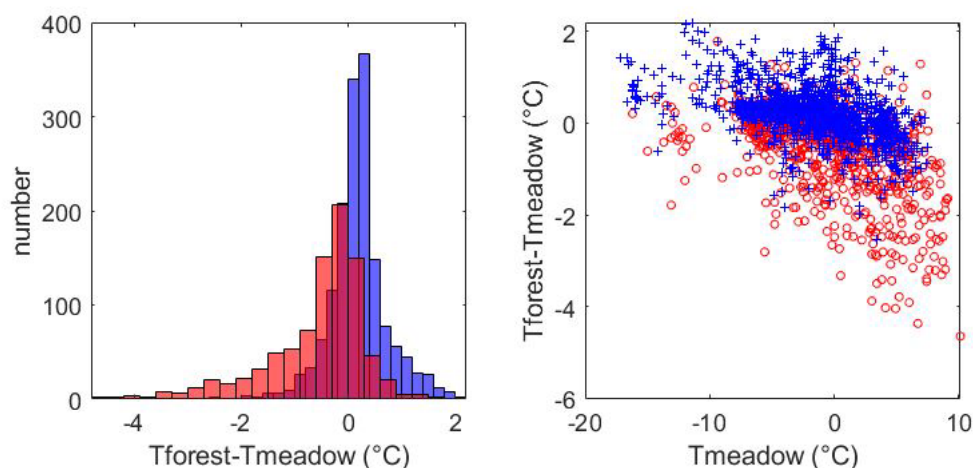
285

286   Figure 11: difference of hourly air temperature between forest and meadow (T_{forest}-T_{meadow}) during the 2018 campaign. The

287   distinction between daytime (red bars and circles) and nigthtime (blue bars and crosses) values is based on a threshold on the

288   shortwave incoming radiation fluxes in the meadow site ($SW < 10$ W m^{-2} during nightime).

289

290   Figures 12 and 13 illustrate the spatial variability of snow depth and snow water equivalent measurements in the open meadow

291   and along the snow pole transect in the forest (see locations in Figure 1) during the 2017 and 2018 field campaigns. As

292   previously mentioned, snow cover lasted several weeks longer and was deeper in the second campaign than in the first, reaching

293   a maximum in the meadow of 160 cm and 100 cm, respectively. The seasonal maximum snow depth under the canopy was

294   smaller than that of the meadow by factors ranging from 0.20 to 0.75, depending on the local canopy cover. For the snow water

295   equivalent, these ratios ranged from 0.16 to 0.60. Relative decreases in snow depth and water equivalent in the forest transect

296   compared to the meadow were greater during the first campaign characterized by shallow snow cover. Figures 12 and 13

297   suggest that the effects of the forest on snow cover are more marked during the winter accumulation season (likely due to

298   interception of snow by the canopy), whereas melt rates during the short ablation season appear to be quite similar in the forest

299   and the meadow. However, further analysis of snow and meteorological data is required to investigate this point.

300
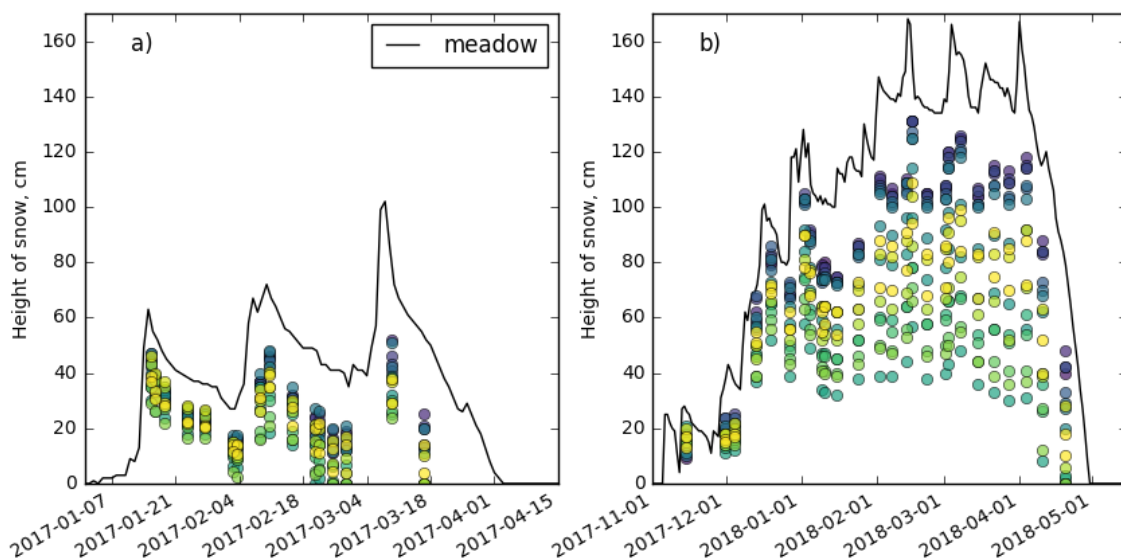
Figure 12: Reference snow depth measured in the meadow from Lejeune et al., 2019 (black line) and manually measured at the snow poles transect in the forest (circles, each color corresponds to a snow pole) during the 2017 (a) and the 2018 (b) field campaigns.
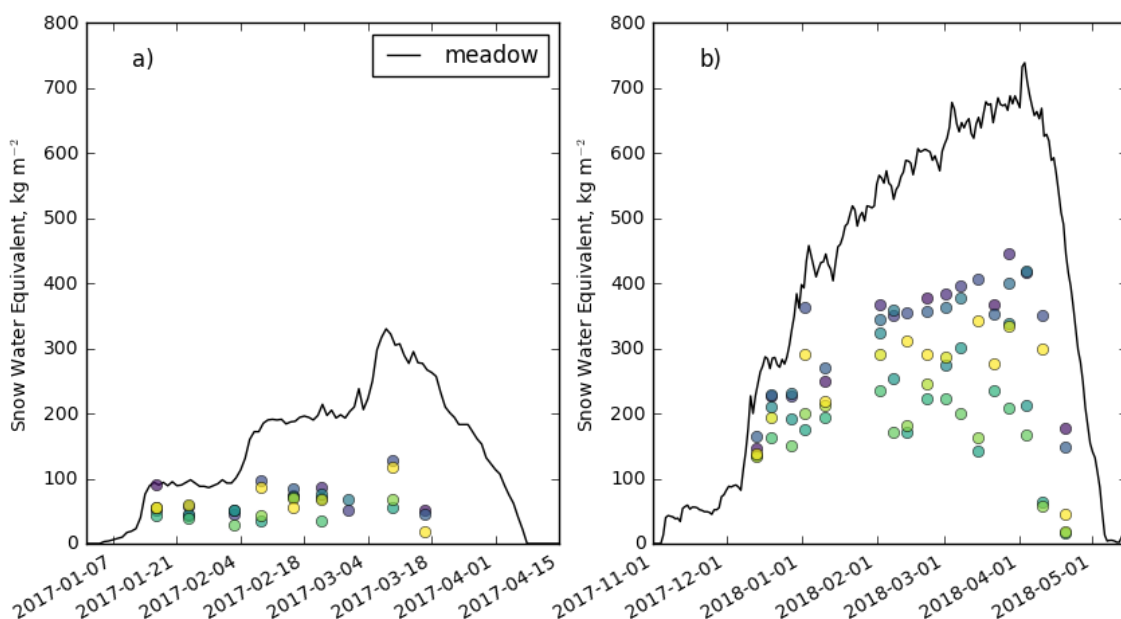
Figure 13: Reference Snow Water Equivalent measured in the meadow site with cosmic ray neutron sensor (black line, see details in Lejeune et al., 2019) and manually measured at the snow poles transect in the forest (circles, each color corresponds to a snow pole) during the 2017 (a) and the 2018 (b) field campaigns.

17

Earth System
Science
Data

310

311 Table 2: Link to the dataset repository.

Data set	Period	Format	Repository
Forest inventory	13-14 September 2016 27 July 2018	csv	https://doi.osug.fr/data/public/SNOUF/forest/
Hemispherical photographs	4 September 2017	png	https://doi.osug.fr/data/public/SNOUF/hemis-photos/
Rugged laser scan	22 Feb to 4 April 2017 5 Dec 2017 to 13 May 2018	netCDF	https://doi.osug.fr/data/public/SNOUF/laser-scan/
Airborne laser scanning	30 August and 2 September 2016	100	https://doi.osug.fr/data/public/SNOUF/lidar/
Weather station and radiometer array measurements	16 Jan 2016 to 14 June 2022	csv	https://doi.osug.fr/data/public/SNOUF/meteo/
Snow pole and precipitation tank measurements	16 Jan 2016 to 21 March 2017 1 Dec 2017 to 15 March 2018	xls	https://doi.osug.fr/data/public/SNOUF/snow/

312

3 Conclusions

314 The datasets collected in the Col de Porte coniferous forest will allow research on the effects of the canopy on snow
315 accumulation and ablation processes under different canopy covers. Two intensive field campaigns were conducted during the
316 winters of 2016-17 and 2017-18 and an automatic weather station has been maintained under the canopy since then.
317 Meteorological and snow measurements (automatic weather station, radiometer array, snow pole transect, laser scan,
318 precipitation tanks to estimate snow interception by the canopy) were complemented by canopy observations (tree inventory,
319 LIDAR measurements of forest structure, sub-canopy hemispherical photographs). Continuous measurements throughout the
320 year at high temporal frequency (15-minute) from the meteorological station allow hydrological and ecological studies related
321 to seasonal changes in micrometeorological and soil conditions.

Data availability

323 All datasets described and presented in this paper can be openly accessed from the repository of the Observatoire des Sciences
324 de l'Univers de Grenoble (OSUG) data center at: http://dx.doi.org/10.17178/SNOUF.2022 (Sicart et al., 2022). Table 2
325 provides the links to the different datasets.

Open Access
Earth System
Science
Data
Discussions

326 **Author contributions**

327 JES organized the data and wrote the first draft of the manuscript. JMM and YL cleaned and corrected the forest and snow

328 measurements, respectively. LA and GP cleaned and corrected the laser scan measurements. VR and DS analyzed the

329 meteorological data. All authors participated to the field campaigns, collected and assembled data records, and contributed to

330 writing the paper.

331 **Competing interests**

332 The authors declare that they have no conflict of interest.

333 **Disclaimer**

334 Any reference to specific equipment types or manufacturers is for informational purposes and does not represent a product

335 endorsement.

336 **Acknowledgments and funding**

340 **References**

341 Boone, A., Samuelsson, P., Gollvik, S., Napoly, A., Jarlan, L., Brun, E., and Decharme, B.: The interactions between soil-

342 biosphere-atmosphere land surface model with a multi-energy balance (ISBA-MEB) option in SURFEXv8-Part 1: Model

343 description, Geosci. Model Dev., 10, 843-872, 10.5194/gmd-10-843-2017, 2017.

344 Durot, K., Modélisation hydrologique distribuée du bassin versant nivo-pluvial de Sarennes. Validation des données d'entrées

345 et dévelopement d'un module de fonte nivale sous forêt, PhD. thesis, Laboratoire d'Etude des Transferts en Hydrologie et

346 Environnement, UJF, 332 pp.., 1999.

347 Ellis, C. R., Pomeroy, J. W., and Link, T. E.: Modeling increases in snowmelt yield and desynchronization resulting from forest

348 gap-thinning treatments in a northern mountain headwater basin, Water Resources Research, 49, 936-949,

349 10.1002/wrcr.20089, 2013.

350 Elzinga, C., Shearer, R. C., and Elzinga, G.: Observer Variation in Tree Diameter Measurements, Western Journal of Applied

351 Forestry, 20, 134-137, 10.1093/wjaf/20.2.134, 2005.

352 Essery, R.: Large-scale simulations of snow albedo masking by forests, Geophysical Research Letters, 40, 5521-5525, 2013.

353 Essery, R., Bunting, P., Rowlands, A., Rutter, N., Hardy, J., Melloh, R., Link, T., Marks, D., and Pomeroy, J.: Radiative transfer

354   modeling of a coniferous canopy characterized by airborne remote sensing, J. Hydrometeorol., 9, 228-241, 2008.

355 Essery, R., Rutter, N., Pomeroy, J., Baxter, R., Stahli, M., Gustafsson, D., Barr, A., Bartlett, P., and Elder, K.: An Evaluation of

356   Forest Snow Process Simulations, Bull. Amer. Meteorol. Soc., 90, 1120-1136, 10.1175/2009bams2629.1, 2009.

357 Gouttevin, I., Lehning, M., Jonas, T., Gustafsson, D., and Molder, M.: A two-layer canopy model with thermal inertia for an

358   improved snowpack energy balance below needleleaf forest (model SNOWPACK, version 3.2.1, revision 741), Geosci. Model

359   Dev., 8, 2379-2398, 10.5194/gmd-8-2379-2015, 2015.

360 Halldin, S., and A. Lindroth: Errors in Net Radiometry: Comparison and Evaluation of Six Radiometer Designs, Journal of

361   Atmospheric and Oceanic Technology, 9(6), 762-783, 1992.

362 Helbig, N., Moeser, D., Teich, M., Vincent, L., Lejeune, Y., Sicart, J. E., and Monnet, J. M.: Snow processes in mountain forests:

363   interception modeling for coarse-scale applications, Hydrology and Earth System Sciences, 24, 2545-2560, 10.5194/hess-24-

364   2545-2020, 2020.

365 Hojatimalekshah, A., Uhlmann, Z., Glenn, N. F., Hiemstra, C. A., Tennant, C. J., Graham, J. D., Spaete, L., Gelvin, A., Marshall,

366   H. P., McNamara, J. P., and Enterkine, J.: Tree canopy and snow depth relationships at fine scales with terrestrial laser

367   scanning, The Cryosphere, 15, 2187-2209, 10.5194/tc-15-2187-2021, 2021.

368 Jonas, T., Webster, C., Mazzotti, G., and Malle, J.: HPEval: A canopy shortwave radiation transmission model using high-

369   resolution hemispherical images, Agric. For. Meteorol., 284, 9, 10.1016/j.agrformet.2020.107903, 2020.

370 Lejeune, Y., Dumont, M., Panel, J.-M., Lafaysse, M., Lapalus, P., Le, E., Gac, B. L., and Morin, S.: 57 years (1960-2017) of

371   snow and meteorological observations from a mid-altitude mountain site (Col de Porte, France, 1325 m alt.), Earth System

372   Science Data Discussions, 2018, 1-25, 2019.

373 López-Moreno, J. I., Leppänen, L., Luks, B., Holko, L., Picard, G., Sanmiguel-Vallelado, A., Alonso-González, E., Finger, D.

374   C., Arslan, A. N., and Gillemot, K.: Intercomparison of measurements of bulk snow density and water equivalent of snow

375   cover with snow core samplers: Instrumental bias and variability induced by observers, Hydrological Processes, 34, 3120-

376   3133, 2020.

377 Luoma, V., Saarinen, N., Wulder, M. A., White, J. C., Vastaranta, M., Holopainen, M., and Hyyppä, J.: Assessing Precision in

378   Conventional Field Measurements of Individual Tree Attributes, Forests, 8, 38, 2017.

379 Malle, J., Rutter, N., Mazzotti, G., and Jonas, T.: Shading by Trees and Fractional Snow Cover Control the Subcanopy Radiation

380   Budget, Journal of Geophysical Research: Atmospheres, 124, 3195-3207, 10.1029/2018jd029908, 2019.

381 Mazzotti, G., Essery, R., Moeser, C. D., and Jonas, T.: Resolving Small-Scale Forest Snow Patterns Using an Energy Balance

382   Snow   Model   With   a   One-Layer   Canopy,   Water   Resources   Research,   56,   e2019WR026129,

383   https://doi.org/10.1029/2019WR026129, 2020.

384   Mazzotti, G., Currier, W. R., Deems, J. S., Pflug, J. M., Lundquist, J. D., and Jonas, T.: Revisiting Snow Cover Variability and
385   Canopy Structure Within Forest Stands: Insights From Airborne Lidar Data, Water Resources Research, 55, 6198-6216,
386   10.1029/2019wr024898, 2019.

387   Michel, D., et al.: Performance and uncertainty of CNR1 net radiometers during a one-year field comparison, Journal of
388   Atmospheric and Oceanic Technology, 25(3), 442-451, 2008.

389   Morin, S., Lejeune, Y., Lesaffre, B., Panel, J. M., Poncet, D., David, P., and Sudul, M.: An 18-yr long (1993-2011) snow and
390   meteorological dataset from a mid-altitude mountain site (Col de Porte, France, 1325m alt.) for driving and evaluating
391   snowpack models, Earth Syst. Sci. Data, 4, 13-21, 10.5194/essd-4-13-2012, 2012.

392   Musselman, K. N., Molotch, N. P., Margulis, S. A., Lehning, M., and Gustafsson, D.: Improved snowmelt simulations with a
393   canopy model forced with photo-derived direct beam canopy transmissivity, Water Resources Research, 48, 2012.

394   Otterman, J., Staenz, K., Itten, K. I., and Kukla, G.: Dependence of Snow Melting and Surface-Atmosphere Interactions on the
395   Forest Structure, Bound.-Layer Meteor., 45, 1-8, 10.1007/bf00120812, 1988.

396   Philipona, R., et al.: Atmospheric longwave irradiance uncertainty: Pyrgeometers compared to an absolute sky-scanning
397   radiometer, atmospheric emitted radiance interferometer, and radiative transfer model calculations, Journal of Geophysical
398   Research-Atmospheres, 106(D22), 28129-28141, 2001.

399   Picard, G., Arnaud, L., Panel, J. M., and Morin, S.: Design of a scanning laser meter for monitoring the spatio-temporal evolution
400   of snow depth and its application in the Alps and in Antarctica, The Cryosphere, 10, 1495-1511, 2016.

401   Pomeroy, J., Rowlands, A., Hardy, J., Link, T., Marks, D., Essery, R., Sicart, J. E., and Ellis, C.: Spatial Variability of Shortwave
402   Irradiance for Snowmelt in Forests, J. Hydrometeorol., 9, 1482-1490, 10.1175/2008jhm867.1, 2008.

403   Reid, T., Essery, R., Rutter, N., and King, M.: Data-driven modelling of shortwave radiation transfer to snow through boreal
404   birch and conifer canopies, Hydrological Processes, 28, 2987-3007, 2014.

405   Rutter, N., Essery, R., Pomeroy, J., Altimir, N., Andreadis, K., Baker, I., Barr, A., Bartlett, P., Boone, A., Deng, H. P., Douville,
406   H., Dutra, E., Elder, K., Ellis, C., Feng, X., Gelfan, A., Goodbody, A., Gusev, Y., Gustafsson, D., Hellstrom, R., Hirabayashi,
407   Y., Hirota, T., Jonas, T., Koren, V., Kuragina, A., Lettenmaier, D., Li, W. P., Luce, C., Martin, E., Nasonova, O., Pumpanen,
408   J., Pyles, R. D., Samuelsson, P., Sandells, M., Schadler, G., Shmakin, A., Smirnova, T. G., Stahli, M., Stockli, R., Strasser, U.,
409   Su, H., Suzuki, K., Takata, K., Tanaka, K., Thompson, E., Vesala, T., Viterbo, P., Wiltshire, A., Xia, K., Xue, Y. K., and
410   Yamazaki, T.: Evaluation of forest snow processes models (SnowMIP2), J. Geophys. Res.-Atmos., 114, 18, D06111,
411   10.1029/2008jd011063, 2009.

412   Sicart et al. : Snow Under Forest. Snow, forest and meteorological measurements at Col de Porte, SNOUF-OSUG [data set],
413   http://dx.doi.org/10.17178/SNOUF.2022, 2022.

414   Van den Broeke, M., et al.: Surface radiation balance in Antarctica as measured with automatic weather stations, Journal of
415   Geophysical Research, 109(D09103), doi:10.1029/2003JD004394, 2004.

416   Vincent, L.: Observation and modélisation du manteau neigeux sous une forêt d'épicéas au Col de Porte, Thèse de Master 2,
417   Université Paul Sabatier, Toulouse, 40 pp., 2018.

418 Vionnet, V., Brun, E., Morin, S., Boone, A., Faroux, S., Le Moigne, P., Martin, E., and Willemet, J. M.: The detailed snowpack
419   scheme Crocus and its implementation in SURFEX v7. 2, Geosci. Model Dev., 5, 773-791, 2012.
420 Webster, C., Rutter, N., Zahner, F., and Jonas, T.: Modeling subcanopy incoming longwave radiation to seasonal snow using air
421   and tree trunk temperatures, Journal of Geophysical Research: Atmospheres, 121, 1220-1235, 2016.